

REALISTIC PATTERN FORMATIONS ON SURFACES BY ADDING ARBITRARY ROUGHNESS*

SIQING LI[†], LEEVAN LING[‡], STEVEN J. RUUTH[§], AND XUEMENG WANG[¶]

Abstract. We are interested in generating surfaces with arbitrary roughness and forming patterns on the surfaces. Two methods are applied to construct rough surfaces. In the first method, some superposition of wave functions with random frequencies and angles of propagation are used to get periodic rough surfaces with analytic parametric equations. The amplitude of such surfaces is also an important variable in the provided eigenvalue analysis for the Laplace-Beltrami operator and in the generation of pattern formation. Numerical experiments show that the patterns become irregular as the amplitude and frequency of the rough surface increase. For the sake of easy generalization to closed manifolds, we propose a second construction method for rough surfaces, which uses random nodal values and discretized heat filters. We provide numerical evidence that both surface construction methods yield comparable patterns to those observed in real-life animals.

Key words. Laplace-Beltrami operator, reaction-diffusion system, random surfaces, Turing pattern

MSC codes. 65M06, 35K57

1. Introduction. Pattern formation by reaction-diffusion systems has been an intensively studied field for decades. In 1952, Turing proposed the idea of diffusion-driven instability [50], wherein simple mechanisms evolve from a homogeneous state into spatial heterogeneous patterns. In recent years, various application areas have been actively developed, including vegetation patterns, plant root hair initiation, flock formation and boundary drop configurations [4, 7, 14, 33]. Mechanisms of pattern generation under different types of transport or domain size have been explored [6, 26]. In theoretical biology, reaction-diffusion systems provide a relatively generic and concise approach for generating animal skin patterns [19, 36], as well as regenerative processes of organisms [22]. In particular, reaction-diffusion systems are a well-accepted class of models for multiple pigmentation processes, including emperor angelfish [27], genets [1], plecostomi [13], cheetah [49] patterns, which are shown in Figure 1.1, as well as marine angelfish [28], zebra fish [2], and various mammal skin patterns [37]. Although animal skin pattern through reaction-diffusion systems has been explored in many researches, see the second row of Figure 4.2 for typical examples, very few studies have considered the skin texture. In reality, the skin surfaces are often rugged, resulting in patterns that are not strictly characterized by regular spots or stripes. Therefore, combining surface properties with reaction-diffusion systems can provide an opportunity for improving generation of real patterns. In [12, 31], parameter functions instead of constants were used in PDEs to generate nonuniform and complex

*Submitted revised version to the editors: October, 2023.

Funding: This work was funded by the Hong Kong Research Grant Council GRF Grants (12303818, 12301419, 12301520, 12301021), a National Youth Science Foundation of China (12201449), and the financial support of NSERC Canada (RGPIN-2022-03302).

[†]College of Mathematics, Taiyuan University of Technology, Shanxi, China (lisiqing@tyut.edu.cn).

[‡]Department of Mathematics, Hong Kong Baptist University, Kowloon Tong, Hong Kong (lling@hkbu.edu.hk).

[§]Department of Mathematics, Simon Fraser University, Burnaby, British Columbia, Canada V5A1S6 (sruuth@sfu.ca).

[¶]Department of Mathematics, University of British Columbia, Vancouver, Canada, and Department of Mathematics, Hong Kong Baptist University, Kowloon Tong, Hong Kong (17251109@life.hkbu.edu.hk).



FIG. 1.1. *Real-life examples of skin patterns.*

patterns that closely resemble real-life patterns.

Characterizing random rough surfaces can be achieved by a variety of methods. These include the reference parameter method, motif method, fractal method, watershed method, and wavelet method, etc [44]. For three-dimensional surface topography, there are a number of parameters involved [21]. To generate random rough surfaces, two commonly used methods are the Fast Fourier Transform (FFT) [39] and digital filter [24] methods. These methods approximate the auto-correlation function for surfaces with wavelengths. In [25], the authors proposed an approach that applies the covariance function and Karhunen-Loève expansion to generate random surfaces. Alternatively, rough surfaces can also be generated from spatial frequencies via the FFT method by summing up trigonometric functions [45].

Moving from a flat geometry to rough surfaces generally leads to surface dependent differential operators. Surface PDEs have been extensively studied in recent years, and various techniques exist for their analysis and computation. The approaches for surface PDEs can be categorized as extrinsic, embedding, and intrinsic methods. Extrinsic methods solve PDEs on the manifold directly. Some extrinsic methods depend on surface mesh construction. Examples of such methods include finite difference [42], finite element [5, 17, 38], and finite volume [15, 16] methods. Additionally, there are numerical methods that do not require meshes, known as meshfree methods. Meshfree methods for surface PDEs, such as radial basis function (RBF) methods [9, 10, 20] and the meshfree generalized finite difference method [46, 48], have the advantage of avoiding mesh construction. On the other hand, embedding methods [11, 34] formulate and solve PDEs on a band around the manifold. In this paper, intrinsic methods [8, 47] are used, which work on parameter spaces of (local) parametrization.

Our paper focuses on the construction of surfaces with arbitrary roughness and the generation of patterns by solving PDEs on surfaces. In Section 2, the rough surface \mathcal{M} with parametric equations will be formulated in detail. We consider periodic rough surfaces \mathcal{M} characterized with spatial frequency, which are accompanied by analytic parametric equations. The eigenvalue analysis for the Laplace-Beltrami operator is provided. Along with the construction of rough surfaces, Section 3 reviews the intrinsic concept of the surface heat equation, which is a PDE involving the Laplace-Beltrami operator defined by Riemannian metric. We apply the finite differ-

ence method to solve the heat equations, which is chosen because of its simplicity and effectiveness on the class of problem domains considered. In Section 4, we employ the finite difference method to solve pattern formation PDEs on rough surfaces \mathcal{M} . Our aim is to study the effect of roughness on pattern formation using the simplest setup. Numerical experiments for the approximation of pattern formation on rough surfaces \mathcal{M} with parametric equations are demonstrated. Results for PDEs with constant parameters on rough surfaces with various roughness are similar to the real-life patterns displayed in Figure 1.1. The rough surface pattern formation models here are not yet extendable to add roughness to other manifolds; e.g., we cannot yet create red-blood cells with rough surfaces. In Section 5, we present an alternative construction method of rough surfaces \mathcal{S} by random discrete data and discretized heat filters. After updating our numerical schemes for \mathcal{M} to work on \mathcal{S} , we observe that surface types \mathcal{M} and \mathcal{S} yield comparable patterns and animal coats. Furthermore, the proposed surface construction technique can be readily extended to introduce “roughness” to more general manifolds. For instance, it can be applied to generate red-blood cells with rough surfaces.

2. Rough surfaces \mathcal{M} with analytic parametric equations. We consider \mathcal{C}^k -smooth ($k \geq 2$), codimension 1, and periodic Riemannian surfaces, which can be described as

$$(2.1) \quad \mathcal{M} = \{(x, y, z) \in \mathbb{R}^3 : z = z(x, y) \text{ for } (x, y) \in V \subset \mathbb{R}^2\},$$

for some \mathcal{C}^k function $z(\cdot, \cdot)$ defined on a global parameter space $V \subset \mathbb{R}^2$. A corresponding parametric representation of \mathcal{M} is given by

$$\vec{r}(x, y) = [x, y, z(x, y)]^T \in \mathcal{M}, \quad (x, y) \in V.$$

For convenience, we will interchangeably use (x, y) and (x_1, x_2) to refer to the parameters. Recall that the first fundamental form $G : V \rightarrow \mathbb{R}^{2 \times 2}$ of \mathcal{M} is defined by

$$G(x, y) = \begin{bmatrix} g_{11} & g_{12} \\ g_{21} & g_{22} \end{bmatrix} (x, y) \quad \text{where} \quad g_{ij}(x, y) = \frac{\partial \vec{r}(x, y)}{\partial x_i} \cdot \frac{\partial \vec{r}(x, y)}{\partial x_j};$$

see [17] for a review. In the case of a surface function \mathcal{M} as in (2.1), we have

$$(2.2) \quad G(x, y) = \begin{bmatrix} g_{11} & g_{12} \\ g_{21} & g_{22} \end{bmatrix} (x, y) = \begin{bmatrix} 1 + z_x^2 & z_x z_y \\ z_x z_y & 1 + z_y^2 \end{bmatrix},$$

whose determinant and inverse are

$$(2.3) \quad g(x, y) := \det(G)(x, y) = 1 + z_x^2 + z_y^2,$$

and

$$(2.4) \quad G^{-1}(x, y) = \begin{bmatrix} g^{11} & g^{12} \\ g^{21} & g^{22} \end{bmatrix} (x, y) = \frac{1}{1 + z_x^2 + z_y^2} \begin{pmatrix} 1 + z_y^2 & -z_x z_y \\ -z_x z_y & 1 + z_x^2 \end{pmatrix}.$$

Using (2.3)–(2.4), the Laplace-Beltrami operator on \mathcal{M} is given by

$$(2.5) \quad \Delta_{\mathcal{M}} f = \frac{1}{\sqrt{g}} \sum_{1 \leq i, j \leq 2} \frac{\partial}{\partial x_i} \left(\sqrt{g} g^{ij} \frac{\partial}{\partial x_j} f \right) =: \frac{1}{\sqrt{g}} \nabla \cdot (\mathcal{A} \nabla f),$$

for any \mathcal{C}^2 function $f : \mathcal{M} \rightarrow \mathbb{R}$.

Now, our focus shifts to random rough surfaces $\mathcal{M} \subseteq \mathbb{R}^3$ described in the form of (2.1), where the surface function $z : \mathcal{I}^2 = [-L, L]^2 \rightarrow \mathbb{R}$ is a superposition of elementary waves [18, 45]. The function z is stochastically determined by

$$(2.6) \quad z(x, y) = \sum_{m=-M}^M \sum_{n=-N}^N a_{m,n} \cos\left(2\pi(mx + ny) + \phi_{m,n}\right),$$

for some random variables $a_{m,n}$ and $\phi_{m,n}$. Similar to a Fourier series expansion, $z(x, y)$ in (2.6) is constructed by trigonometric functions, where m, n correspond to spatial frequencies on the x and y axes, respectively. As in [45], the spatial frequencies m and n allow values taken up to maximum integers M and N , respectively. This corresponds to a high frequency cut off.

To determine (2.6), we first introduce $\tilde{a}_{m,n} \sim \mathcal{N}(0, 1)$ and $\phi_{m,n} \sim \mathcal{U}(0, \pi)$. This specifies the pre-surface function $\tilde{z} = \tilde{z}(x, y)$. Next, we control the amplitude of the rough surface \mathcal{M} to be within a specific range $[-\delta_{\mathcal{M}}, \delta_{\mathcal{M}}]$ by scaling according to

$$(2.7) \quad z := \frac{\delta_{\mathcal{M}}}{\|\tilde{z}\|_{\infty}} \tilde{z}, \quad \text{i.e., } a_{m,n} := \frac{\delta_{\mathcal{M}}}{\|\tilde{z}\|_{\infty}} \tilde{a}_{m,n}.$$

Figures 2.1 (a)–(c), first column, show some rough surfaces \mathcal{M} with amplitude $\delta_{\mathcal{M}} = 10^{-3}$ and various (M, N) . The construction of the rough surfaces \mathcal{S} appearing in the second column will be discussed in Section 5.

Remark: One can also add a decay condition with respect to frequencies m, n and a frequency attenuation parameter β to the pre-coefficient $\tilde{a}_{m,n}$ via

$$\tilde{a}_{m,n} \sim \frac{1}{(m^2 + n^2)^{\beta/2}} \mathcal{N}(\mu, \sigma).$$

2.1. Surface roughness and Laplace-Beltrami operator. Applying the definition of the Laplace-Beltrami operator in (2.5) to the rough surface function in (2.6)–(2.7), the relationship between the eigenvalues of the diffusion tensor and the geometry of the surface can be made explicit. Firstly, the *diffusion tensor* \mathcal{A} in (2.5) is

$$(2.8) \quad \mathcal{A}(x, y) = \begin{bmatrix} \mathcal{A}_1 & \mathcal{A}_2 \\ \mathcal{A}_2 & \mathcal{A}_4 \end{bmatrix} (x, y) := \sqrt{g} G^{-1} = \frac{1}{\sqrt{g}} \begin{bmatrix} 1 + z_y^2 & -z_x z_y \\ -z_x z_y & 1 + z_x^2 \end{bmatrix},$$

with the partial derivatives z_x and z_y computing from (2.6). We are interested in obtaining the eigenvalues and eigenvectors of \mathcal{A} . Instead of computing these quantities directly, it turns out to be easier to first compute the eigenvalues and eigenvectors of the Riemannian metric tensor G in (2.2). From the characteristic equation of G

$$|G - \lambda I| = (1 + z_x^2 - \lambda)(1 + z_y^2 - \lambda) - z_x^2 z_y^2 = 0,$$

we find that the eigenvalues λ^G of G are $1 + z_x^2 + z_y^2 = g$ and 1. Since

$$(2.9) \quad \mathcal{A}\vec{v} = \sqrt{g} G^{-1} \vec{v} = \frac{\sqrt{g}}{\lambda^G} \vec{v},$$

any eigenvector \vec{v} of G is also an eigenvector of \mathcal{A} , and the eigenvalues $\lambda^{\mathcal{A}}$ of \mathcal{A} are

$$(2.10) \quad \lambda^{\mathcal{A}} = \left\{ \sqrt{g} = \sqrt{1 + z_x^2 + z_y^2}, \frac{1}{\sqrt{g}} \right\}.$$

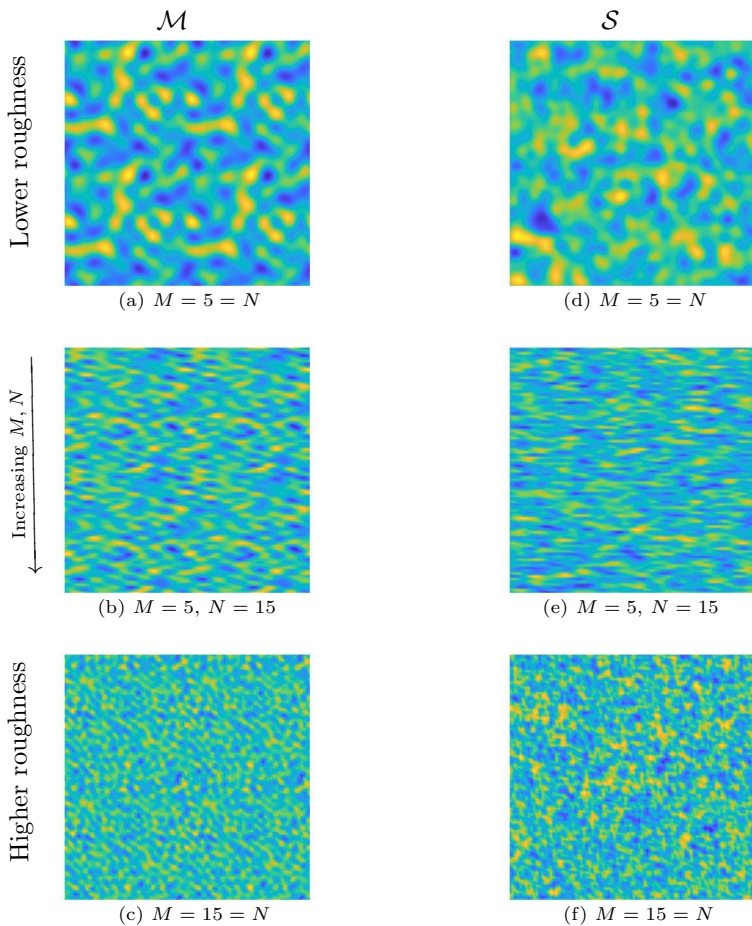


FIG. 2.1. A bird's-eye view depicting random rough surfaces \mathcal{M} (left) by the construction method from Section 2 and \mathcal{S} (right) by the construction method from Section 5 .

Note that, by (2.7), the matrix function $[G - \lambda^G I](z_x, z_y) = C(\delta_{\mathcal{M}})[G - \lambda^G I](\tilde{z}_x, \tilde{z}_y)$ for some $\delta_{\mathcal{M}}$ -dependent constant $C(\delta_{\mathcal{M}})$. This implies that all eigendirections of G (and \mathcal{A}) are independent of the amplitude $\delta_{\mathcal{M}}$. Simple calculations show that $\lambda^{\mathcal{A}} = 1 + \mathcal{O}(M^2 N^2 \delta_{\mathcal{M}}^2)$ varies with $\delta_{\mathcal{M}}$ nonlinearly by a bijection. Thus, the contour lines (but not the height) of $\lambda^{\mathcal{A}}$ are independent of $\delta_{\mathcal{M}}$.

Figure 2.2 illustrates the close relationship between the eigenvalues of \mathcal{A} and the geometric properties of a rough surface. In particular, when examining subfigures (b), (c), and (e), it becomes evident that the maximum (and minimum) eigenvalues are larger (and smaller) at regions of the surface with the steepest gradients. In subfigures (d) and (f), eigendirections are plotted on top of subfigure (b). We can clearly see that the eigenvectors corresponding to the maximum (and minimum) eigenvalues are tangent (and orthogonal) to the contour plots of eigenvalues. By adding roughness to the computational domain, an isotropic diffusion problem will become anisotropic and directionality of gradients in the solution will appear. Eigen-directions associated with large eigenvalues are preferred directions.

3. Solving heat equations on rough surfaces \mathcal{M} . We begin by constructing a finite difference scheme for solving heat equations on rough surfaces $\mathcal{M} \subset \mathbb{R}^3$ defined

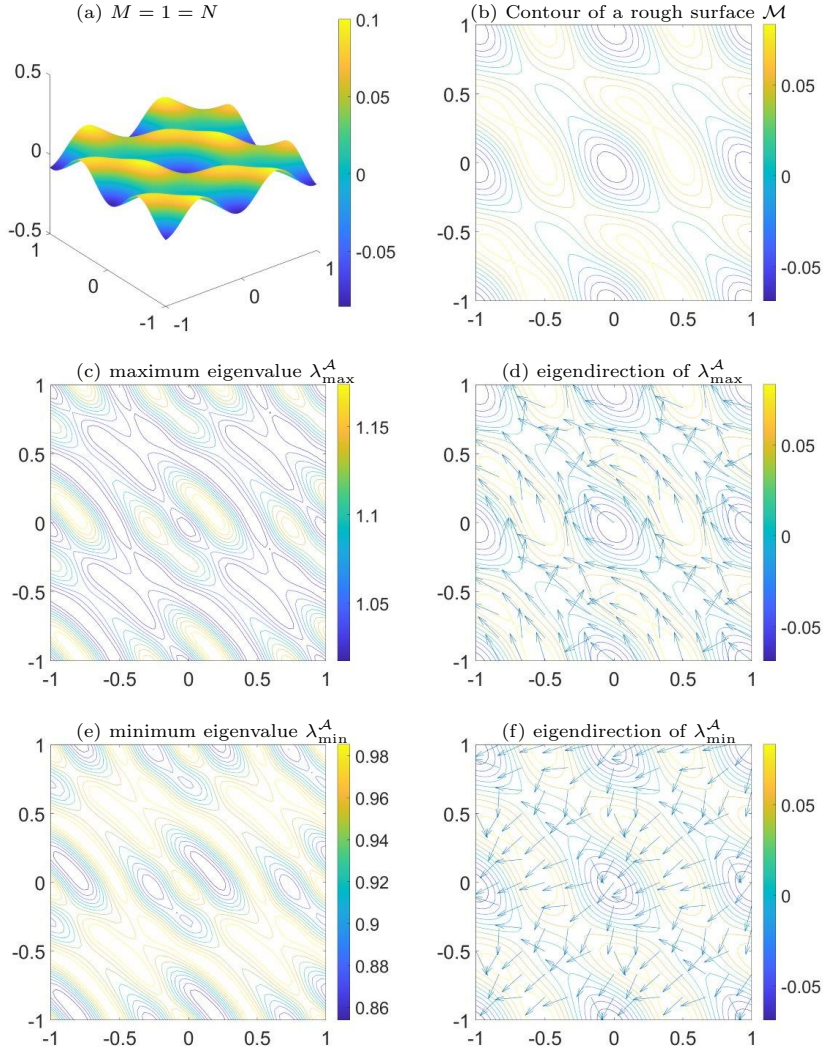


FIG. 2.2. (a, b): 3D and contour plots of a rough surface characterized by (2.7) with $M = N = 1$ and amplitude $\delta_{\mathcal{M}} = 1E - 1$; (c, d): maximum eigenvalue and corresponding eigendirection of \mathcal{A} , (e, f): minimum eigenvalue and corresponding eigendirection of \mathcal{A} .

by (2.6)–(2.7). We work intrinsically by transforming the PDEs on rough surfaces to the parameter space $\mathcal{I}^2 = [-L, L]^2 \subset \mathbb{R}^2$. Subsequently, we move on to solving reaction-diffusion systems for pattern formation.

We consider the heat equation on a rough surface described by

$$(3.1a) \quad \frac{\partial u}{\partial t}(\boldsymbol{\xi}, t) - \Delta_{\mathcal{M}} u(\boldsymbol{\xi}, t) = h(\boldsymbol{\xi}, t) \quad \text{for } \boldsymbol{\xi} \in \mathcal{M}, t \in (0, T],$$

where $u : \mathcal{M} \times (0, T] \rightarrow \mathbb{R}$, subject to periodic boundary conditions on $\partial\mathcal{M} := \partial\mathcal{I}^2 \times z(\partial\mathcal{I}^2)$ with $z(\partial\mathcal{I}^2)$ being the surface function in (2.6), i.e.,

$$(3.1b) \quad \begin{aligned} u([-L, y, z(-L, y)]^T, t) &= u([L, y, z(L, y)]^T, t), & \text{for } y \in \mathcal{I}, t \in (0, T], \\ u([x, -L, z(x, -L)]^T, t) &= u([x, L, z(x, L)]^T, t), & \text{for } x \in \mathcal{I}, t \in (0, T]. \end{aligned}$$

Since all surface points are in the form $\xi = [x, y, z(x, y)]^T \in \mathcal{M}$ for $[x, y]^T \in \mathcal{I}^2$ and z in (2.6), we discretize the parameter space \mathcal{I}^2 by some set of $n_X n_Y$ tensor-product grid points, $[X, Y] \in \mathbb{R}^{n_X n_Y \times 2} \subset \mathcal{I}^2$. Let $u^j(x, y) \approx u([x, y, z(x, y)]^T, t^j)$ for $[x, y]^T \in \mathcal{I}^2$. We begin by temporal discretization of (3.1a) by the θ -method

$$(3.2) \quad \frac{u^{j+1} - u^j}{\tau} = \theta(\Delta_{\mathcal{M}} u^{j+1} + h^{j+1}) + (1 - \theta)(\Delta_{\mathcal{M}} u^j + h^j),$$

for an equispaced partition $\{t^j\}_{j=0}^M$ of $[0, T]$ with a step-size τ . By some user-selected finite difference scheme for the first derivative, we construct differentiation matrices $\mathcal{D}_k \in \mathbb{R}^{n_X n_Y \times n_X n_Y}$ such that, for any C^1 -function $w : \mathcal{I}^2 \rightarrow \mathbb{R}$ satisfying periodic boundary condition (3.1b), we have

$$\mathcal{D}_k w(X, Y) \approx \frac{\partial w}{\partial x_k}(X, Y), \quad \text{for } k \in \{1, 2\},$$

where the $n_X n_Y \times 1$ vector $w(X, Y)$ (and $\frac{\partial w}{\partial x_k}(X, Y)$) contains nodal values of w (and $\frac{\partial w}{\partial x_k}$) at grid points in $[X, Y]$. By working directly on the definitions (2.5)–(2.8), we can approximate the Laplace-Beltrami term $\Delta_{\mathcal{M}} w$ at grids $[X, Y]$ by nodal function values $W := w(X, Y)$ as follows:

$$(3.3) \quad \begin{aligned} \Delta_{\mathcal{M}} w(X, Y) &\approx \frac{1}{\sqrt{g}}(X, Y) \otimes \left(\mathcal{D}_1 \left(\mathcal{A}_1(X, Y) \otimes (\mathcal{D}_1 W) \right) + \mathcal{D}_2 \left(\mathcal{A}_4(X, Y) \otimes (\mathcal{D}_2 W) \right) \right. \\ &\quad \left. + \mathcal{D}_1 \left(\mathcal{A}_2(X, Y) \otimes (\mathcal{D}_2 W) \right) + \mathcal{D}_2 \left(\mathcal{A}_2(X, Y) \otimes (\mathcal{D}_1 W) \right) \right) \\ &= \frac{1}{\sqrt{g}}(X, Y) \otimes \left[\mathcal{D}_1 \left(\mathcal{A}_1(X, Y) \otimes \mathcal{D}_1 \right) + \mathcal{D}_2 \left(\mathcal{A}_4(X, Y) \otimes \mathcal{D}_2 \right) \right. \\ &\quad \left. + \mathcal{D}_1 \left(\mathcal{A}_2(X, Y) \otimes \mathcal{D}_2 \right) + \mathcal{D}_2 \left(\mathcal{A}_2(X, Y) \otimes \mathcal{D}_1 \right) \right] W \\ &=: \Delta_{\mathcal{M}, h} W, \end{aligned}$$

where $\Delta_{\mathcal{M}, h} \in \mathbb{R}^{n_X n_Y \times n_X n_Y}$, \otimes is the element-wise Hadamard product of matrices and \odot is a vector-matrix product defined as $\vec{a} \odot [\vec{b}_1, \dots, \vec{b}_n] := [\vec{a} \otimes \vec{b}_1, \dots, \vec{a} \otimes \vec{b}_n]$. See the Appendix for the detailed construction of differentiation matrices $\mathcal{D}_1, \mathcal{D}_2$. Combining (3.2) and (3.3) yields a fully discretized scheme for the update in time.

To verify the accuracy and convergence of the introduced finite difference scheme, we consider a heat equation with a known exact solution. The parameter space is set to be $\mathcal{I}^2 = [-1, 1]^2$. The exact solution is $u^*(x, y, t) = \exp(t) \sin(\pi x) \sin(\pi y)$. The function $f(x, y, t)$ and initial condition are generated from the exact solution u^* . In all cases, we use the backward Euler method. Periodic boundary conditions are imposed. The relative ℓ^2 -error at t^n is computed as

$$(3.4) \quad \ell^2\text{-error} = \frac{\|u_N^n - u^*\|_2}{\|u^*\|_2}.$$

For the surface $M = N = 1$ in Figure 2.2 (a) with $\delta_M = 1E-2$, Figure 3.1 (a) exhibits second order spatial convergence for $n_X, n_Y \in \{5, 10, \dots, 40\}$, $\tau = 1E-3$, $T = 1E-1$. Figure 3.1 (b) exhibits first order convergence with respect to time for $n_X = 90 = n_Y$, $\tau \in \{1/2, 1/2^2, \dots, 1/2^6\}$, $T = 1$.

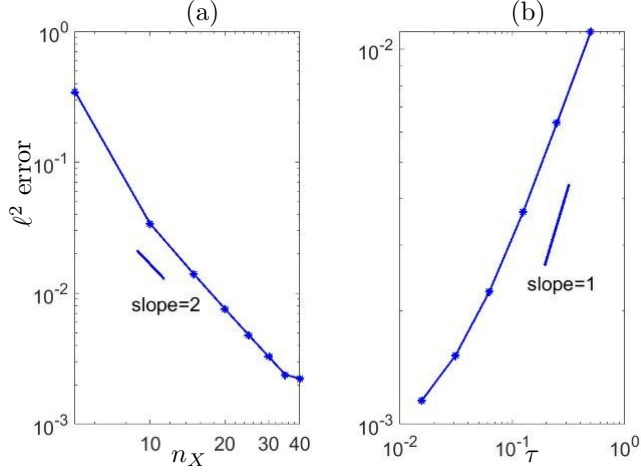


FIG. 3.1. Accuracy and convergence results for the heat equation on the rough surface in Figure 2.2(a) with $M = N = 1, \delta_M = 1E - 2$: (a) Convergence with respect to spatial refinement. (b) Convergence with respect to time.

3.1. Visualizing heat flow on a rough surface \mathcal{M} . We visualize the heat flow under different amplitudes of rough surface \mathcal{M} in Figure 2.2 by solving the heat equations (3.1a) with zero flux $h(\xi, t) = 0$ and periodic boundary conditions (3.1b). The rough surfaces \mathcal{M} are defined over the parameter space $\mathcal{I}^2 = [-1, 1]^2 \subset \mathbb{R}^2$. The compatible initial condition is given by

$$(3.5) \quad u(x, y, z, 0) = \cos(\pi x/2) \cos(\pi y/2).$$

Figure 3.2 shows the numerical solutions on the surface \mathcal{M} in Figure 2.2 (b) with $\delta_M \in \{0.1, 0.5, 1\}$ in the respective rows. In all cases, we set $\tau = 1E - 3$, $T = 1$ and $n_X = 41 = n_Y$. Figure 3.2 shows that the range of the numerical solutions becomes larger as the amplitude of \mathcal{M} increases from $\delta_M = 0.1$ to $\delta_M = 1$. From the rough surface in Figure 2.2 (b) and solutions in Figure 3.2, it can be concluded that the heat flow, when projected onto the plane, is greatest in flat regions.

4. Pattern formation on a rough surface \mathcal{M} . In this section, we examine reaction-diffusion systems (RDS) on a rough surface \mathcal{M} , given by

$$(4.1) \quad \begin{cases} \partial_t u = \delta_u \Delta_{\mathcal{M}} u + f_u(u, v), \\ \partial_t v = \delta_v \Delta_{\mathcal{M}} v + f_v(u, v), \end{cases}$$

for some (concentration) functions $u, v : \mathcal{M} \times (0, T] \rightarrow \mathbb{R}$, and reaction terms

$$(4.2) \quad \begin{cases} f_u(u, v) = \alpha u(1 - \xi_1 v^2) + v(1 - \xi_2 u), \\ f_v(u, v) = \beta v \left(1 + \frac{\alpha \xi_1}{\beta} uv \right) + u(\gamma + \xi_2 v), \end{cases}$$

with parameters $\delta_u, \delta_v, \alpha, \beta, \xi_1, \xi_2$. Pattern formation on very smooth (and usually closed) surfaces with little variation has been discussed in [11, 30, 35, 43]. However, to the best of the authors' knowledge, the study of pattern formation on rough surfaces has not been undertaken. In this section, we aim to analyze the effect of rough surfaces on pattern formation generated by the reaction-diffusion system (4.1)-(4.2). We are

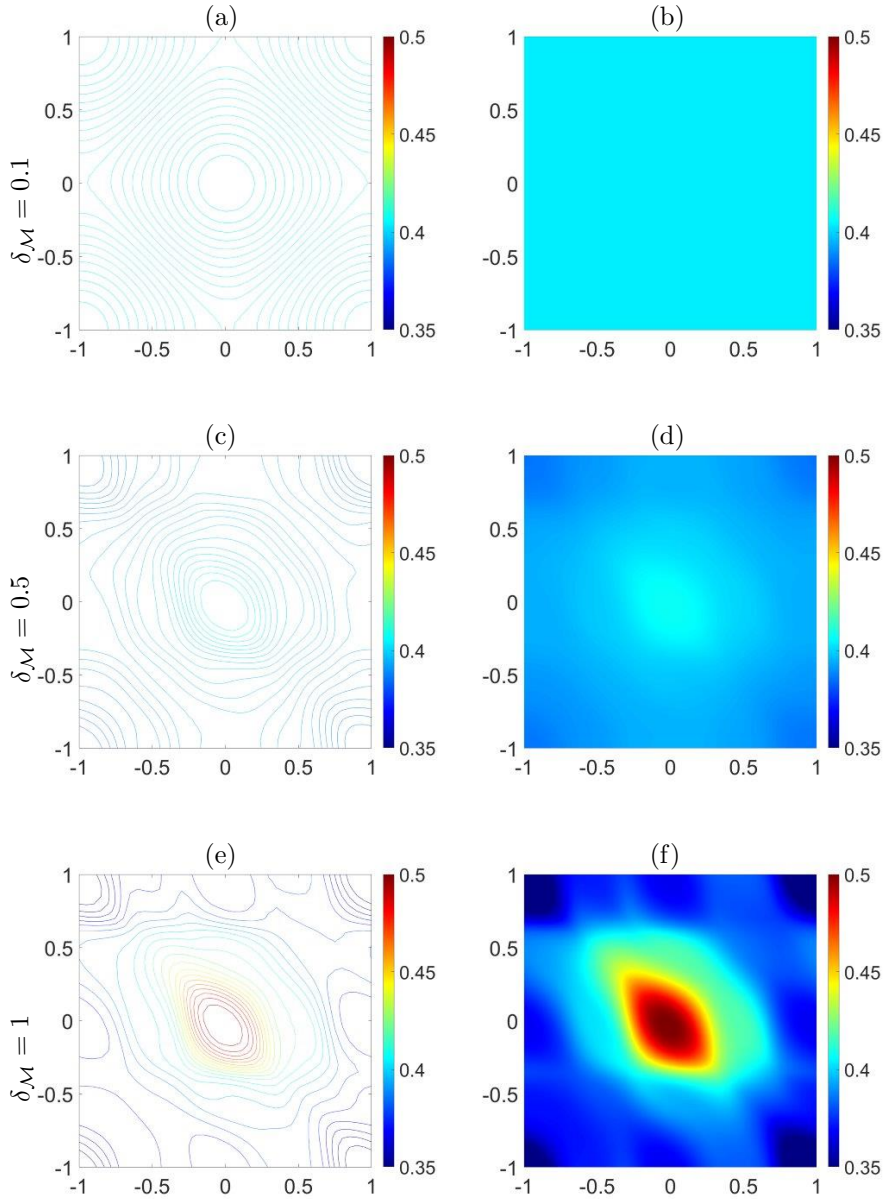


FIG. 3.2. Numerical investigation of heat equation solutions on \mathcal{M} with varying amplitudes $\delta_{\mathcal{M}}$: (a, b): $\delta_{\mathcal{M}} = 0.1$, (c, d): $\delta_{\mathcal{M}} = 0.5$, (e, f): $\delta_{\mathcal{M}} = 1$. In all cases, $\tau = 1E-3$, $T = 1$, $n_X = 41 = n_Y$.

not primarily focused on numerical methods, and simply extend the finite difference scheme from the previous section to work here. Other options for discretizing reaction-diffusion systems include the finite element method [23, 29, 40], and various types of meshfree methods [31, 32].

As in Section 3, we work on an equispaced temporal partition $\{t^j\}_{j=0}^{N_T}$ with some

time step $\tau > 0$ and tensor-product grid points $[X, Y] \in \mathbb{R}^{n_X n_Y \times 2} \subset \mathcal{I}^2$. Let

$$U^j \approx u(X, Y, z(X, Y), t^j) \quad \text{and} \quad V^j \approx v(X, Y, z(X, Y), t^j), \quad 1 \leq j \leq N_T,$$

be the unknown nodal values we seek based on initial conditions U^0 and V^0 . Using the second order backward differentiation formula (BDF2) [3, 41] and (3.3) to discretize the RDS (4.1) with periodic boundary condition (3.1b), we obtain the following fully-discrete system of equations on \mathcal{M}

$$(4.3) \quad \begin{cases} 3U^{j+1} - 2\tau\delta_u\Delta_{\mathcal{M},h}U^{j+1} = 4\tau f_u(U^j, V^j) - 2\tau f_u(U^{j-1}, V^{j-1}) + 4U^j - U^{j-1}, \\ 3V^{j+1} - 2\tau\delta_v\Delta_{\mathcal{M},h}V^{j+1} = 4\tau f_v(U^j, V^j) - 2\tau f_v(U^{j-1}, V^{j-1}) + 4V^j - V^{j-1}, \end{cases}$$

for $1 \leq j \leq N_T$, subject to some yet-to-be specified (usually random) initial condition and some first order approximations to the solutions at the first time step, U^1 and V^1 . Note that the two equations in (4.3) are not coupled, and the computational cost is of the same order as that of solving two scalar heat equations. Here, we compute the RDS with exact solutions to demonstrate the convergence behavior of the finite difference scheme. The parametric domain is chosen to be $\mathcal{I}^2 = [-1, 1]^2$. The exact solutions are

$$u^*(x, y, t) = \exp(t) \sin(2\pi x) \sin(\pi y), \quad v^*(x, y, t) = \exp(t) \sin(\pi x) \sin(2\pi y).$$

In order to obtain RDS with these exact solutions, we construct new reaction functions $F_u(u, v)$ and $F_v(u, v)$ as

$$F_u(u, v) = f_u(x, y, t) + f_u(u, v), \quad F_v(u, v) = f_v(x, y, t) + f_v(u, v),$$

with

$$\begin{aligned} f_u(x, y, t) &= \frac{\partial u^*(x, y, t)}{\partial t} - \delta_u \Delta_{\mathcal{M}} u^*(x, y, t) - f_u(u^*, v^*), \\ f_v(x, y, t) &= \frac{\partial v^*(x, y, t)}{\partial t} - \delta_v \Delta_{\mathcal{M}} v^*(x, y, t) - f_v(u^*, v^*). \end{aligned}$$

Periodic boundary conditions are imposed and initial conditions are generated from the exact solution u^*, v^* . The relative ℓ^2 -errors at t^n are computed by those of u and v as in (3.4) according to

$$\ell^2\text{-error} = \frac{\sqrt{(\ell^2\text{-error of } u)^2 + (\ell^2\text{-error of } v)^2}}{n_E}.$$

We consider the surface in Figure 2.2 (a) with $M = N = 1$ and $\delta_M = 1E - 2$. In Figure 4.1 (a), we observe second order spatial convergence for $n_X, n_Y \in \{10, 15, \dots, 40\}$, $\tau = 1E - 3$, $T = 1E - 1$. Figure 4.1 (b) shows second order convergence in time for $n_X = 90 = n_Y$, $\tau \in \{1/2, 1/2^2, \dots, 1/2^6\}$, $T = 1$.

4.1. The pattern generation process. In this subsection, we show the formation of irregular patterns as we transition from a flat two dimensional domain to rough surfaces with varying amplitudes. We begin with patterns on the flat domain $[-1, 1]^2$ as in [31], i.e., the rough surface with zero amplitude ($\delta_{\mathcal{M}} = 0$). The model and surface parameters are determined based on the values in Table 4.1. For discretization,

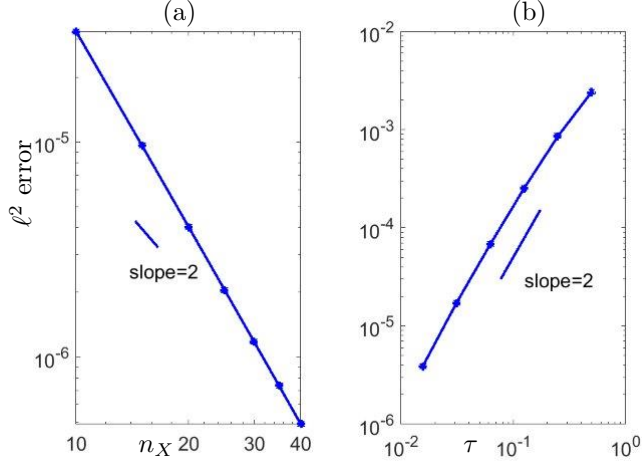


FIG. 4.1. Accuracy and convergence results for a reaction-diffusion system on the rough surface in Figure 2.2(a) with $M = N = 1, \delta_M = 1E-2$. (a) Convergence with respect to spatial refinement. (b) Convergence with respect to time.

TABLE 4.1

Parameters of the reaction-diffusion system (4.1)-(4.2) for generating spots and stripes patterns on rough surfaces.

Pattern	δ_v	δ_u	α	β	γ	ξ_1	ξ_2
Spots	10^{-3}	$0.516\delta_v$	0.899	-0.91	-0.899	0.02	0.2
Stripes	10^{-3}	$0.516\delta_v$	0.899	-0.91	-0.899	3.5	0

we select grid parameters $n_X = 90, n_Y = n_X$, and a time step-size $\tau = 0.5$. The rough surfaces \mathcal{M} with $M = N = 5$ are used in this part.

The first row of Figure 4.2 plots the initial conditions used to compute the spots and stripes patterns, respectively. These are random values generated within the interval $[-0.5, 0.5]$. The second row of Figure 4.2 shows the steady state patterns on the surface with zero amplitude. Perfect spots and stripes are obtained, similar to our previous results in [31]. Next, we set the initial conditions for the next amplitude to be the steady solutions from the zero amplitude rough surface. In other words, we use the solution of spots with $\delta_M = 0, T = 800$ and the solution of stripes with $\delta_M = 0, T = 4000$. By increasing the amplitude of the rough surface from $\delta_M = 0$ to $\delta_M = 0.1$ with increments of 0.01, and setting initial conditions using the previous steady state, we achieve the final patterns for $\delta_M = 0.1$. These are shown in the third row of Figure 4.2. For rough surfaces under a small amplitude $\delta_M = 0.05$, the spots and stripes are similar to those with $\delta_M = 0$. However, for a larger amplitude $\delta_M = 0.1$, both spots and stripes become irregular. From this, we can conclude that the steady state patterns become irregular as the amplitude of the rough surface \mathcal{M} increases.

4.2. Patterns on surfaces with different spatial frequencies and amplitudes. Properties of rough surfaces are influenced by the amplitude δ_M and the spatial frequencies M, N in (2.7). To better understand patterns on rough surfaces with different properties, we compute steady state patterns for

$$\delta_M \in \{0.05, 0.1\}, \quad (M, N) \in \{(5, 15), (15, 15)\},$$

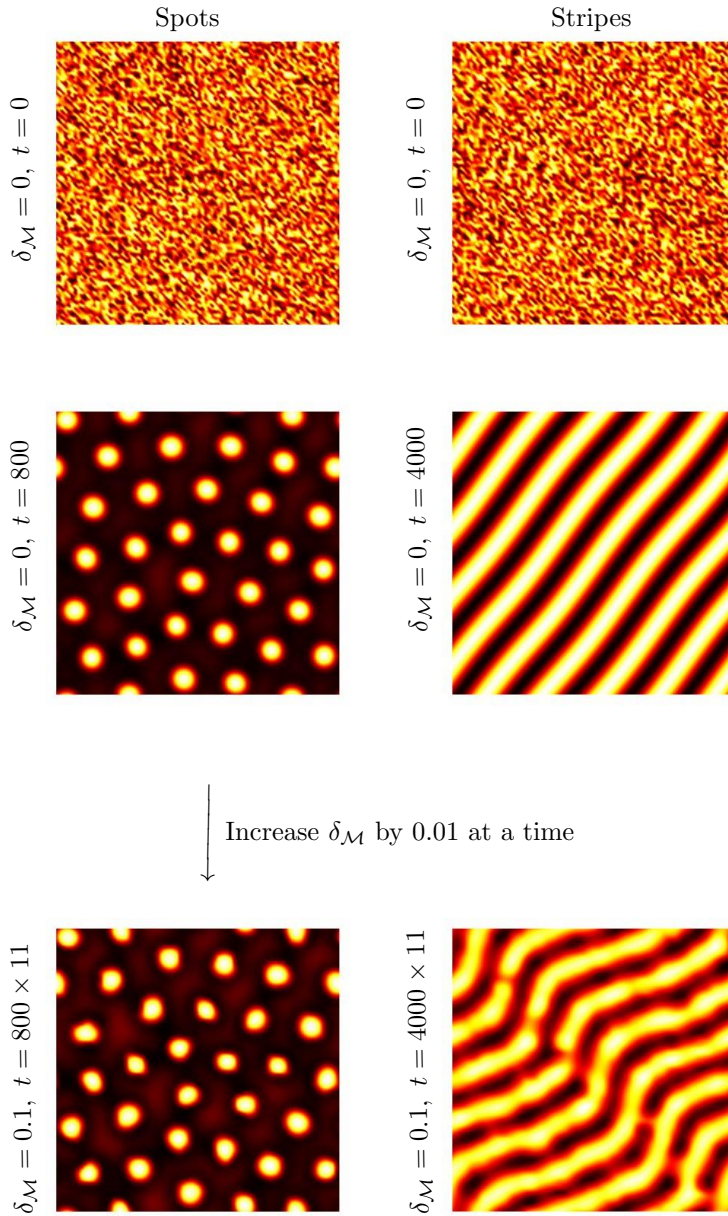


FIG. 4.2. Pattern generation on rough surfaces \mathcal{M} with $M = N = 5$ and amplitude $\delta_{\mathcal{M}}$ increasing from 0 to 0.1. Parameters for spots and stripes are set according to Table 4.1. The discretization sets as $n_X = 90 = n_Y$, $\tau = 0.5$.

on the parameter space $\mathcal{I}^2 = [-0.5, 0.5]^2 \subset \mathbb{R}^2$. Periodic boundary conditions on $\partial\mathcal{M} := \partial\mathcal{I}^2 \times z(\partial\mathcal{I}^2)$ are prescribed.

These patterns, both 2-D view and zoom in 3-D view, are presented in Figures 4.3–4.4 for spots, and in Figures 4.5–4.6 for stripes. As before, the initial conditions are assigned to be random data in $[-0.5, 0.5]$. In order to capture details of the spot and stripe patterns, we increase the spatial resolution from $n_X = 90$ to

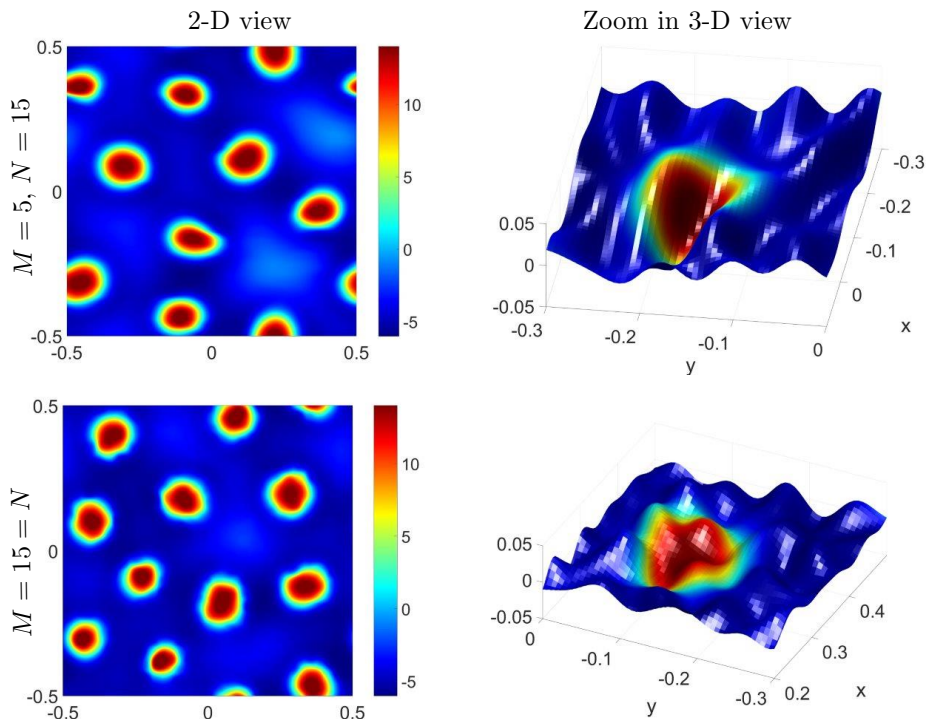


FIG. 4.3. Pattern formation on rough surfaces with an amplitude $\delta_{\mathcal{M}} = 0.05$. Discretization parameters are $n_X = 170 = n_Y$, $\tau = 0.5$, $T = 800$, $\mathcal{I}^2 := [-0.5, 0.5]^2$.

$n_X = 170$, again keeping $n_Y = n_X$ to ensure the irregular patterns are due to the roughness rather than low resolution.

Firstly, from Figures 4.3 and 4.4, we can see that the number of spots increases as the frequencies M, N and the amplitude $\delta_{\mathcal{M}}$ increase. For a fixed amplitude $\delta_{\mathcal{M}}$, patterns undergo deformation along the x -axis as the frequency N increases. This observation is particularly evident in the case $\delta_{\mathcal{M}} = 0.1$. On the other hand, for fixed values of M, N , the patterns maintain their spot shapes when $\delta_{\mathcal{M}} \leq 0.05$, and start to deform when $\delta_{\mathcal{M}} \geq 0.05$. When $\delta = 0.1$, all patterns become deformed spots.

Secondly, for a fixed $\delta_{\mathcal{M}} = 0.05$, zoom in 3-D profiles of region $[-0.3, 0.1] \times [-0.3, 0]$ for $[M, N] = [5, 15]$ and region $[0.2, 0.5] \times [-0.3, 0]$ for $[M, N] = [15, 15]$ reveal that irregular spots appear when part of the pattern is situated in a valley or ridge of the rough surface. When $\delta_{\mathcal{M}}$ increases to 0.1, as in Figure 4.4, the deformation of the patterns is more severe. This is because the amplitude $\delta_{\mathcal{M}}$ here is twice of that in Figure 4.3. From zoom in 3-D figures of region $[-0.1, 0.5] \times [0.1, 0.4]$ for $[M, N] = [5, 15]$ and region $[-0.4, 0.1] \times [-0.2, 0.1]$ for $[M, N] = [15, 15]$, the deformed patterns again appear when their locations cover the local ridge/valley/mountain of the rough surfaces.

When frequencies and amplitudes are varied, similar behavior (to the case of spots) can be observed in stripe formation, see Figures 4.5 and 4.6. High amplitudes and frequencies yield a particularly strong effect in the zoom in 3-D plots displayed in Figure 4.6, where the stripes break into small separate components. Further, we observe that the largest concentration values appear at the local peaks of the rough surface \mathcal{M} .

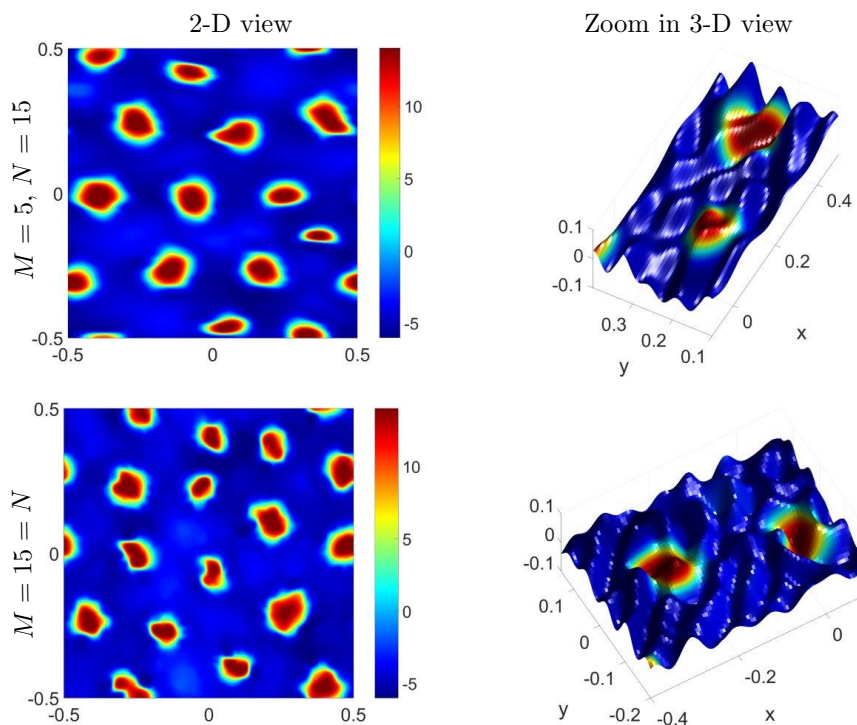


FIG. 4.4. Patterns on rough surfaces \mathcal{M} with an amplitude $\delta_{\mathcal{M}} = 0.1$. Discretization parameters are $n_X = 170 = n_Y$, $\tau = 0.5$, $T = 800$, $\mathcal{I}^2 := [-0.5, 0.5]^2$.

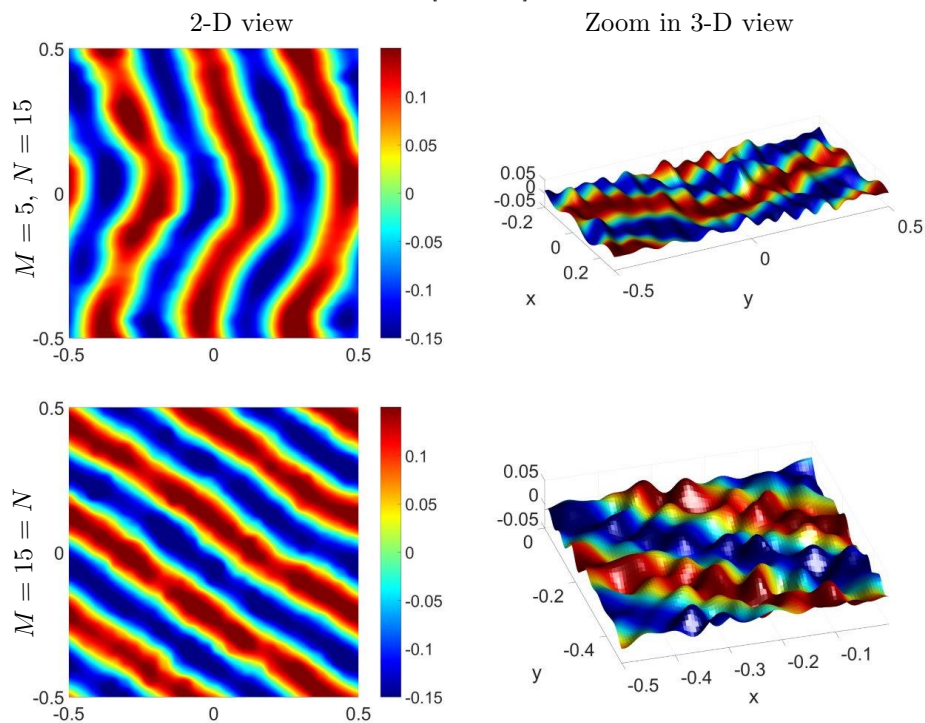


FIG. 4.5. Patterns on rough surfaces \mathcal{M} with an amplitude $\delta_{\mathcal{M}} \in \{0.05\}$ and $(M, N) \in \{(5, 15), (15, 15)\}$. The model parameters for stripes are set according to Table 4.1. Discretization parameters are $n_X = 170 = n_Y$, $\tau = 0.5$, $T = 4000$.

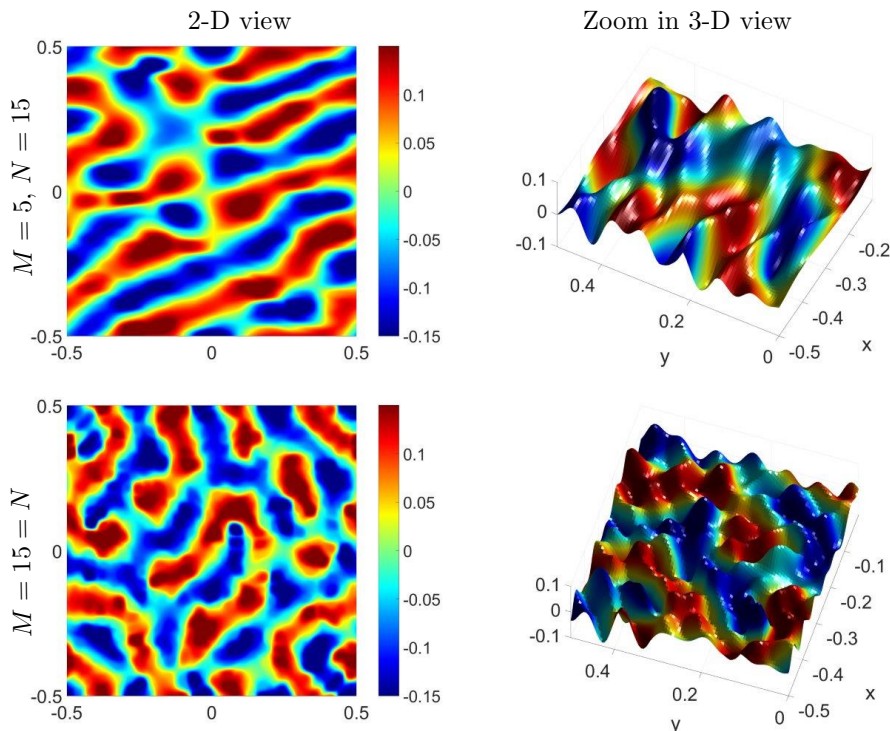


FIG. 4.6. Patterns on rough surfaces \mathcal{M} with an amplitude $\delta_{\mathcal{M}} = 0.1$ and $(M, N) \in \{(5, 15), (15, 15)\}$. The model parameters for stripes are set according to Table 4.1. Discretization parameters are $n_X = 170 = n_Y, \tau = 0.5, T = 4000$.

4.3. Animal coat generation results. When computing results on rough surfaces \mathcal{M} characterized by spatial frequencies, we observe interesting similarities between some steady state patterns and actual animal coat patterns. In Figure 4.7, we show the formation of the animal coats, as in Figure 1.1. These patterns are now on rough surfaces \mathcal{M} . The specific parameter values for generating each animal coat pattern are listed in Tables 4.1 and 4.2.

TABLE 4.2
Parameters for animal coats formation on \mathcal{M} in Figure 4.7 with $n_X = n_Y = 90$

		M	N	τ	T	$\delta_{\mathcal{M}}$
Emperor angelfish [27]	Figure 4.7 (a)	5	5	0.5	4000	0.05
Genet [1]	Figure 4.7 (b)	15	15	0.5	800	0.1
Plecostomus [13]	Figure 4.7 (c)	15	5	0.5	4000	0.1
Cheetah [49]	Figure 4.7 (d)	15	5	0.5	800	0.1

5. Random rough surfaces \mathcal{S} by discrete data. While the parametric equation (2.6) enables us to work analytically on rough surfaces, i.e., via the evaluation of metric tensor (2.2), its generalization to manifolds [10, 11, 42] is not trivial.

In [25], the authors used the covariance function of random deformation fields and the surface Karhunen-Loève expansion to generate random surfaces. In [24], the authors employed 2D digital filters and Fourier analysis to generate random rough surfaces. In this section, we introduce a new approach for constructing rough surfaces

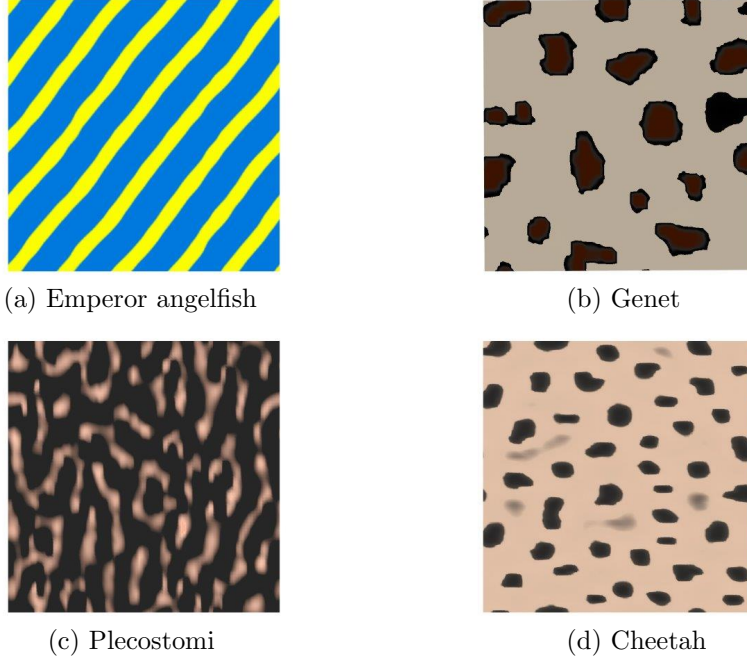


FIG. 4.7. *Experimental results for actual animal coat pattern formations on rough surfaces \mathcal{M} with parameters in Table 4.1 and Table 4.2*

\mathcal{S} based on random data and heat filters. Subsequently, the desired reaction-diffusion systems are then solved on \mathcal{S} .

5.1. Construction of \mathcal{S} by heat filters. We aim to generate some random rough surfaces \mathcal{S} , which have similar roughness as rough surfaces \mathcal{M} in (2.7) with different M and N .

Let $[X, Y] \in \mathbb{R}^{n_X n_Y \times 2} \subset \mathcal{I}^2$ as in Section 3. We assign uniform random numbers to each node to obtain the initial random surface values $\tilde{Z}_0 \sim (\mathcal{U}[-1, 1])^{n_X n_Y}$ at nodes $[X, Y]$. We define the discretized heat filter according to the method outlined in Section 3, but with some filter-diffusion tensor \mathcal{F} (instead of the diffusion tensor \mathcal{A} for surface \mathcal{M}) in the Laplace-Beltrami operator $\Delta_{\mathcal{F}, h}$. For an isotropic filter, we set $\mathcal{F} = I_{2 \times 2}$. This can generate an \mathcal{M} -like surface with $M = N$. For the anisotropic case with $M \neq N$, we use $\mathcal{F} = \text{diag}(2, 1)$. We can now *smooth* the surface data J -times via

$$\tilde{Z}_{j+1} = (Q + \kappa h \Delta_{\mathcal{F}, h}) \tilde{Z}_j, \quad \text{for } j = 0, \dots, J,$$

where Q is an $n_X n_Y$ by $n_X n_Y$ matrix of ones, $\kappa > 0$ is the parameter to control the weights of $\Delta_{\mathcal{F}, h}$, and h is the fill distance of the discrete set. This completes the definition of the pre-surface, that is the counterpart to \tilde{Z} in (2.7) of the surface type \mathcal{M} . Similar to the scaling in (2.7), we define \mathcal{S} solely based on nodal values

$$\left\{ [X, Y, Z] : Z = \frac{\delta_{\mathcal{S}}}{\|\tilde{Z}_J\|_{\infty}} \tilde{Z}_J \right\} \subset \mathcal{S},$$

for some amplitude $\delta_{\mathcal{S}} > 0$.

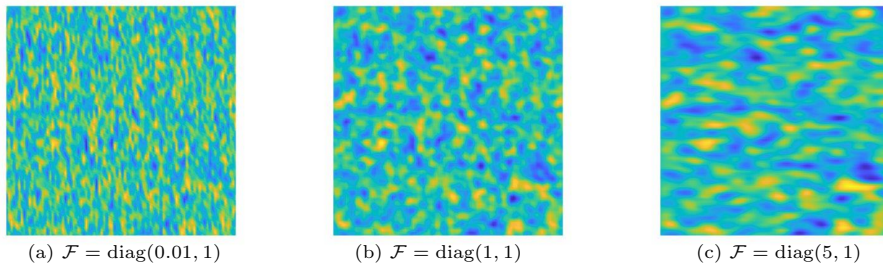


FIG. 5.1. Rough surfaces \mathcal{S} with $\kappa = 2$ and the number of filter steps $J = 15$, subject to different filter-diffusion tensors \mathcal{F} .

TABLE 5.1

Coefficients for constructing the surfaces \mathcal{S} in the second column of Figure 2.1. Parameters are chosen to give qualitative agreement with the rough surfaces \mathcal{M} (2.7) with $\delta_{\mathcal{S}} = 1E-3$, $n_X = 90 = n_Y$

\mathcal{M} in (2.7)	\mathcal{S} by heat filter		
	κ	\mathcal{F}	filter number
$[M, N] = [5, 5]$	5	$\text{diag}(1, 1)$	15
$[M, N] = [5, 15]$	8	$\text{diag}(1, 0.01)$	10
$[M, N] = [15, 15]$	0.2	$\text{diag}(20, 20)$	2

Subfigures of Figure 5.1 show the rough surfaces \mathcal{S} derived for fixed $n_X = 90$, $n_Y = n_X$, $\kappa = 2$ and $J = 15$ filter steps, using different filter-diffusion tensors

$$\mathcal{F} \in \{\text{diag}(0.01, 1), \text{diag}(1, 1), \text{diag}(5, 1)\},$$

respectively. Taking $\mathcal{F}(1, 1) = 1$ yields a rough surface \mathcal{S} which is similar to a rough surface \mathcal{M} with equal frequencies M, N (cf. Figure 2.1). By setting $\mathcal{F}(1, 1) = 0.01$, space is scaled down in the x -direction, yielding a rough surface \mathcal{S} which is similar to a rough surface \mathcal{M} with a larger frequency M , $M > N$. Conversely, when $\mathcal{F}(1, 1) = 5$, a rough surface \mathcal{S} is obtained which resembles \mathcal{M} with a lower frequency M , $M < N$.

To reproduce the properties of surface \mathcal{M} , the required value of filter-diffusion tensors \mathcal{F} and number J of filtering steps will depend on the density of the given data points $[X, Y]$. For fixed amplitude $\delta_{\mathcal{S}} = 1E-3$ and $n_X = 90$, $n_Y = n_X$, Table 5.1 gives values of κ , \mathcal{F} and the number of filtering steps J required to generate surfaces that exhibit good qualitative agreement with the rough surfaces \mathcal{M} in (2.7) for various M, N . Figure 2.1 provides a comparison, demonstrating that rough surfaces \mathcal{S} by heat filters (column 2) are qualitatively similar to our previous surfaces \mathcal{M} by (2.7) (see column 1).

While not the focus of the current work, our construction methods for \mathcal{S} can be extended to generate rough closed manifolds that are suitable for approximating numerical solutions of PDEs. See Figure 5.2 for a graphical illustration of rough closed manifolds generated by type- \mathcal{M} and type- \mathcal{S} construction methods, respectively. Figure 5.2(a) was obtained by applying the type- \mathcal{M} procedure to the parameter space $(\theta, \phi) \in [0, 2\pi] \times [0, \pi]$ with roughness added to the constant function $r = 1$. Figure 5.2(b) was obtained by adding noise to $r = 1$ for points on the unit sphere. In contrast to that in (3.3), the heat filter here makes use of the discrete Laplace-Beltrami operator for the rough sphere.

The FDM in Section 3 can be employed to solve PDEs on rough surfaces \mathcal{S} . The

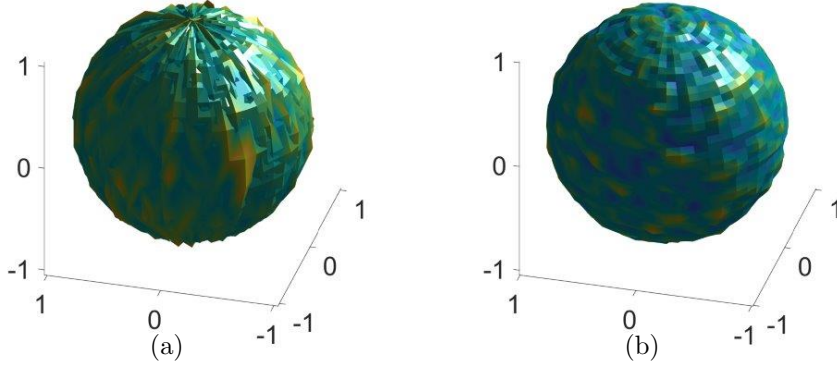


FIG. 5.2. Graphical illustration of rough closed manifolds by (a) type- \mathcal{M} procedure, where roughness is added to the (constant) radius function of the spherical coordinate, and (b) type- \mathcal{S} procedure, where random noise is first added to data points on the unit sphere and then smoothed by heat filter.

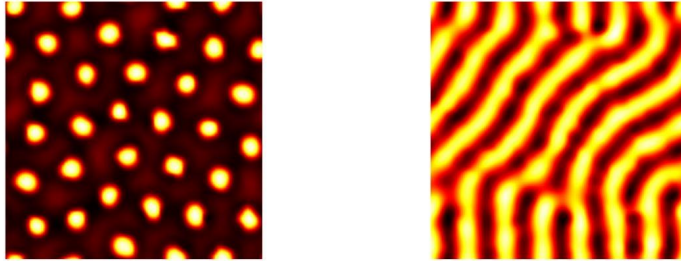


FIG. 5.3. For $\delta_S = 0.1$, $n_X = 90$, $n_Y = n_X$, spot and stripe patterns on a rough surface \mathcal{S} with number of filter steps $J = 15$, $\mathcal{F} = \text{diag}(1, 1)$, and $\kappa = 5$. These values from Table 5.1 give a rough surface similar to \mathcal{M} with $M = 5$, $N = 15$. Parameters for spots and stripes are determined according to Table 4.1.

only difference in the method is that we no longer have the parametric equation to calculate the metric tensor G in (2.2), and hence the diffusion tensor \mathcal{A} in (3.3). Instead of computing metric tensor G analytically as in Sections 3 and 4, centered finite difference formulas are applied to approximate the metric tensor G . For solving reaction-diffusion systems on rough surfaces \mathcal{S} , we set initial conditions to be steady state solutions on a zero amplitude rough surface \mathcal{M} (2.7). Figure 5.3 plots the spot and stripe patterns on a rough surface \mathcal{S} using the reaction-diffusion parameters provided in Table 4.1. As indicated in the second line of Table 5.1, rough surface \mathcal{S} takes $\kappa = 5$, $\mathcal{F} = \text{diag}(1, 1)$ with $J = 15$ filter steps to approximate rough surface \mathcal{M} with $M = 5$, $N = 5$. It is evident that the spot and stripe patterns generated on \mathcal{S} are closely resemble those on \mathcal{M} under parameters $M = 5$, $N = 5$, $\delta_{\mathcal{M}} = 0.1$ (see the third row of Figure 4.2).

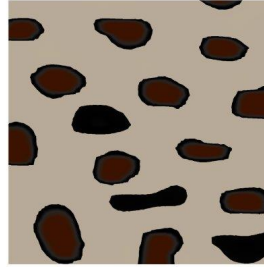
We conclude by generating the same set of animal coats displayed in Figure 1.1 using Turing models on rough surfaces \mathcal{S} with parameters specified in Table 4.1 and Table 5.2. Figure 5.4 demonstrates again that adding surface roughness into the process of pattern generation can indeed provide more varied formations for animal coats. Moreover, the patterns on surface \mathcal{S} exhibit valid formations just like \mathcal{M} .

TABLE 5.2
Parameters for animal coat generation on S with $n_X = n_Y = 90$

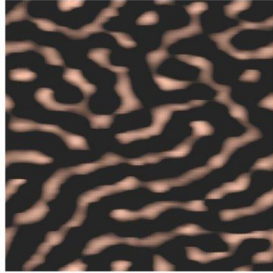
		κ	\mathcal{F}	J	τ	T	δ_S
Emperor angelfish [27]	Figure 5.4 (a)	5	diag(1, 1)	15	0.5	400	0.05
Genet [1]	Figure 5.4 (b)	8	diag(1, 0.01)	10	0.5	800	0.1
Plecostomus [13]	Figure 5.4 (c)	8	diag(1, 0.01)	10	0.5	3000	0.1
Cheetah [49]	Figure 5.4 (d)	0.2	diag(20, 20)	2	0.5	400	0.05



(a) Emperor angelfish



(b) Genet



(c) Plecostomi



(d) Cheetah

FIG. 5.4. Experimental results for actual animal coat pattern formations on rough surfaces S with parameters in Table 4.1 and Table 5.2.

6. Conclusion. In this paper, we discussed the generation of surfaces with arbitrary roughness and the formation of patterns on such surfaces. Rough surfaces are characterized by two different methods: surfaces by analytic parametric equations, and surfaces constructed by imposing discretized heat filters on random nodal values. The patterns generated on random rough surfaces with varying amplitudes and spatial frequencies are illustrated, and the computational results indicate that the patterns became increasingly irregular as amplitude increases. The change of spatial frequencies on the x and y axes also lead to pattern deformation along the corresponding directions. It can be concluded that surface roughness leads to the patterns becoming deformed and of different sizes. Conversely, when the amplitude equals zero, i.e., a flat two dimensional domain, the patterns are regular stripes and spots. We conclude that combining reaction-diffusion systems with rough surfaces gives a way to achieve a better match to the observed variability of patterns in a variety of real world animal coats. Furthermore, the method for generating rough surfaces by heat filters can be further applied to obtain closed rough manifolds. We plan to explore this

generalization in future work.

Appendix: Finite difference algorithm for the heat equation. The heat equation (3.1) on a rough surface defined over the parameter space $\mathcal{I}^2 = [-1, 1]^2$ is considered. The set of discrete data points on \mathcal{I}^2 is defined as:

$$[X, Y] := \left\{ \left\{ (x_1^i, x_2^j) \right\}_{i=1}^{n_X} \right\}_{j=1}^{n_Y} \in \mathbb{R}^{n_X n_Y \times 2},$$

with mesh size h_{x_1}, h_{x_2} on each axis. To fully discretize (3.2), we require discretization of the Laplacian-Beltrami operator. For any twice differentiable function $u : \mathcal{I}^2 \rightarrow \mathbb{R}$, we introduce differentiation matrices $\mathcal{D}_k \in \mathbb{R}^{n_X n_Y \times n_X n_Y}$, $k \in \{1, 2\}$ satisfying periodic boundary condition (3.1b) as follows. Using a second-order centered finite differences, we have for each point (x_1^i, x_2^j) that

$$\begin{aligned} \frac{\partial u}{\partial x_1}(x_1^i, x_2^j) &= \begin{bmatrix} -\frac{1}{2h_{x_1}} & \frac{1}{2h_{x_1}} \end{bmatrix} \begin{bmatrix} u(x_1^{i-1}, x_2^j) \\ u(x_1^{i+1}, x_2^j) \end{bmatrix}, \\ \frac{\partial u}{\partial x_2}(x_1^i, x_2^j) &= \begin{bmatrix} -\frac{1}{2h_{x_2}} & \frac{1}{2h_{x_2}} \end{bmatrix} \begin{bmatrix} u(x_1^i, x_2^{j-1}) \\ u(x_1^i, x_2^{j+1}) \end{bmatrix}. \end{aligned}$$

The following fictitious node approach is applied to handle the periodic boundary conditions:

$$\begin{aligned} u(x_1^0, x_2^j) &= u(x_1^{n_X-1}, x_2^j), \quad u(x_1^{n_X+1}, x_2^j) = u(x_1^2, x_2^j), \quad u(x_1^i, x_2^0) = u(x_1^i, x_2^{n_Y-1}), \\ u(x_1^i, x_2^{n_Y+1}) &= u(x_1^i, x_2^2), \quad u(x_1^1, x_2^j) = u(x_1^{n_X}, x_2^j), \quad u(x_1^i, x_2^1) = u(x_1^i, x_2^{n_Y}). \end{aligned}$$

By assembling all points in $[X, Y]$, the nodal values of $\frac{\partial u}{\partial x_k}$ ($k = 1, 2$) at $[X, Y]$ can be obtained by

$$\frac{\partial u}{\partial x_k}(X, Y) \approx \mathcal{D}_k u(X, Y), \quad \text{for } k \in \{1, 2\},$$

where $u(X, Y) := [u(x_1^1, x_2^1), \dots, u(x_1^{n_X}, x_2^1), \dots, u(x_1^1, x_2^{n_Y}), \dots, u(x_1^{n_X}, x_2^{n_Y})]^T$ is the vector of nodal function values and differential matrices $\mathcal{D}_k \in \mathbb{R}^{n_X n_Y \times n_X n_Y}$ are in the form of

$$\mathcal{D}_1 = \begin{bmatrix} D_1^B & \dots & 0 \\ \vdots & \ddots & \vdots \\ 0 & \dots & D_1^B \end{bmatrix}, \quad D_1^B = \frac{1}{2h_{x_1}} \begin{bmatrix} 0 & 1 & 0 & \dots & 0 & -1 & 0 \\ -1 & 0 & 1 & \dots & 0 & 0 & 0 \\ \vdots & \vdots & \vdots & \ddots & \vdots & \vdots & \\ 0 & 0 & 0 & \dots & -1 & 0 & 1 \\ 1 & 0 & 0 & \dots & 0 & 0 & -1 \end{bmatrix},$$

and

$$\mathcal{D}_2 = \begin{bmatrix} 0 & D_2^B & 0 & \dots & 0 & -D_2^B & 0 \\ -D_2^B & 0 & D_2^B & \dots & 0 & 0 & 0 \\ \vdots & \vdots & \vdots & \ddots & \vdots & \vdots & \vdots \\ 0 & 0 & 0 & \dots & -D_2^B & 0 & D_2^B \\ D_2^B & 0 & 0 & \dots & 0 & 0 & -D_2^B \end{bmatrix}, \quad D_2^B = \frac{1}{2h_{x_2}} \begin{bmatrix} 1 & \dots & 0 \\ \vdots & \ddots & \vdots \\ 0 & \dots & 1 \end{bmatrix},$$

with $D_k^B \in \mathbb{R}^{n_X \times n_X}$, $k \in \{1, 2\}$.

REFERENCES

- [1] <https://commons.wikimedia.org/wiki/Category:Genetta%20tigrina?uselang=it>.
- [2] R. ASAI, E. TAGUCHI, Y. KUME, M. SAITO, AND S. KONDO, *Zebrafish Leopard gene as a component of the putative reaction-diffusion system*, *Mechanisms of Development*, (1999), p. 6.
- [3] U. M. ASCHER AND L. R. PETZOLD, *Computer methods for ordinary differential equations and differential-algebraic equations*, Society for Industrial and Applied Mathematics, 1998.
- [4] D. AVITABILE, V. F. BREÑ MEDINA, AND M. J. WARD, *Spot dynamics in a reaction-diffusion model of plant root hair initiation*, *SIAM Journal on Applied Mathematics*, 78 (2018), pp. 291–319.
- [5] M. BERTALMIÓ, L. CHENG, S. OSHER, AND G. SAPIRO, *Variational problems and partial differential equations on implicit surfaces*, *Journal of Computational Physics*, 174 (2001), pp. 759–780.
- [6] H. A. BROOKS AND P. C. BRESSLOFF, *A mechanism for Turing pattern formation with active and passive transport*, *SIAM Journal on Applied Dynamical Systems*, 15 (2016), pp. 1823–1843.
- [7] P. CARTER AND A. DOELMAN, *Traveling stripes in the klausmeier model of vegetation pattern formation*, *SIAM Journal on Applied Mathematics*, 78 (2018), pp. 3213–3237.
- [8] L. CHARETTE, C. B. MACDONALD, AND W. NAGATA, *Pattern formation in a slowly flattening spherical cap: delayed bifurcation*, *IMA Journal of Applied Mathematics*, 85 (2020), pp. 513–541.
- [9] M. CHEN AND L. LING, *Kernel-based meshless collocation methods for solving coupled bulk-surface partial differential equations*, *Journal of Scientific Computing*, 81 (2019), pp. 375–391.
- [10] ———, *Extrinsic meshless collocation methods for PDEs on manifolds*, *SIAM Journal of Numerical Analysis*, 58 (2020), pp. 988–1007.
- [11] K. C. CHEUNG AND L. LING, *A kernel-based embedding method and convergence analysis for surfaces PDEs*, *SIAM Journal of Scientific Computing*, 40 (2018), pp. A266–A287.
- [12] A. CHU, *Closest point methods with polyharmonic spline radial basis functions and local refinement*, PhD thesis, University of British Columbia, 2021.
- [13] CONTRIBUTORS TO WIKIMEDIA PROJECTS. <https://en.wikipedia.org/wiki/Plecostomus>.
- [14] J. DONG, *Avoiding collisions and pattern formation in flocks*, *SIAM Journal on Applied Mathematics*, 81 (2021), pp. 2111–2129.
- [15] Q. DU, M. D. GUNZBURGER, AND L. JU, *Voronoi-based finite volume methods, optimal Voronoi meshes, and PDEs on the sphere*, *Computer Methods in Applied Mechanics and Engineering*, 192 (2003), pp. 3933–3957.
- [16] Q. DU AND L. JU, *Finite volume methods on spheres and spherical centroidal voronoi meshes*, *SIAM Journal on Numerical Analysis*, 43 (2005), pp. 1673–1692.
- [17] G. DZIUK AND C. M. ELLIOTT, *Finite element methods for surface PDEs*, *Acta Numerica*, 22 (2013), pp. 289–396.
- [18] ———, *The Science of Fractal Images*, vol. 22, Cambridge University Press, 2013.
- [19] P. FIFE, *Mathematical Aspects of Reacting and Diffusing Systems*, *Lecture notes in biomathematics*, Springer-Verlag, 1979.
- [20] E. J. FUSELIER AND G. B. WRIGHT, *A high-order kernel method for diffusion and reaction-diffusion equations on surfaces*, *Journal of Scientific Computing*, 56 (2013), pp. 535–565.
- [21] E. GADELMAWLA, M. KOURA, T. MAKSOU, I. ELEWA, AND H. SOLIMAN, *Roughness parameters*, *Journal of Materials Processing Technology*, 123 (2002), pp. 133–145.
- [22] A. GIERER AND H. MEINHARDT, *A theory of biological pattern formation*, *Kybernetik*, 12 (1972), pp. 30–39.
- [23] G. HU, Z. QIAO, AND T. TANG, *Moving finite element simulations for reaction-diffusion systems*, *Advances in Applied Mathematics and Mechanics*, (2015).
- [24] Y. Z. HU AND K. TONDER, *Simulation of 3-D random rough surface by 2-D digital filter and fourier analysis*, *International journal of machine tools and manufacture*, 32 (1992), pp. 83–90.
- [25] W. HUANG AND M. MULTERER, *Isogeometric analysis of diffusion problems on random surfaces*, arXiv preprint arXiv:2109.03761, (2021).
- [26] V. KLIKA, M. KOZÁK, AND E. A. GAFFNEY, *Domain size driven instability: Self-organization in systems with advection*, *SIAM Journal on Applied Mathematics*, 78 (2018), pp. 2298–2322.
- [27] A. KOK. https://commons.wikimedia.org/wiki/File:Pomocanthus_imperator_facing_right.jpg, 2014.
- [28] S. KONDO AND R. ASAI, *A reaction-diffusion wave on the skin of the marine angelfish pomacanthus*, *Nature*, 376 (1995), pp. 765–768.
- [29] O. LAKKIS, A. MADZVAMUSE, AND C. VENKATARAMAN, *Implicit–explicit timestepping with finite*

- element approximation of reaction–diffusion systems on evolving domains*, SIAM Journal on Numerical Analysis, 51 (2013), p. 2013.
- [30] E. LEHTO, V. SHANKAR, AND G. B. WRIGHT, *A radial basis function (RBF) compact finite difference (FD) scheme for reaction-diffusion equations on surfaces*, SIAM Journal on Scientific Computing, 39 (2017), pp. A2129–A2151.
- [31] S. LI AND L. LING, *Complex pattern formations by spatial varying parameters*, Advances in Applied Mathematics and Mechanics, 12 (2020), pp. 1327–1352.
- [32] S. LI AND Z. QIAO, *A meshless collocation method with a global refinement strategy for reaction-diffusion systems on evolving domains*, Discrete & Continuous Dynamical Systems–B, (2021).
- [33] J. LU, F. BAGINSKI, AND X. REN, *Equilibrium configurations of boundary droplets in a self-organizing inhibitory system*, SIAM Journal on Applied Dynamical Systems, 17 (2018), pp. 1353–1376.
- [34] T. MAERZ AND C. B. MACDONALD, *Calculus on surfaces with general closest point functions*, SIAM J. Numer. Anal., 50 (2012), pp. 3303–3328.
- [35] D. B. MCDONALD, W. J. GRANTHAM, W. L. TABOR, AND M. J. MURPHY, *Global and local optimization using radial basis function response surface models*, Applied Mathematical Modelling, 31 (2007), pp. 2095–2110.
- [36] J. MURRAY, *A pre-pattern formation mechanism for animal coat markings*, Journal of Theoretical Biology, 88 (1981), pp. 161 – 199.
- [37] J. D. MURRAY, *A pattern formation mechanism and its application to mammalian coat markings*, in Vito Volterra Symposium on Mathematical Models in Biology, C. Barigozzi, ed., Berlin, Heidelberg, 1980, Springer Berlin Heidelberg, pp. 360–399.
- [38] M. A. OLSHANSKII, A. REUSKEN, AND J. GRANDE, *A finite element method for elliptic equations on surfaces*, SIAM Journal on Numerical Analysis, 47 (2009), pp. 3339–3358.
- [39] P. PAWLUS, R. REIZER, AND M. WIECZOROWSKI, *A review of methods of random surface topography modeling*, Tribology International, (2020), p. 106530.
- [40] Z. QIAO, *Numerical investigations of the dynamical behaviors and instabilities for the gierer-meinhardt system*, Communications in Computational Physics, 3 (2008), pp. 406–426.
- [41] S. J. RUUTH, *Implicit-explicit methods for reaction-diffusion problems in pattern formation*, Journal of Mathematical Biology, 34 (1994).
- [42] S. J. RUUTH AND B. MERRIMAN, *A simple embedding method for solving partial differential equations on surfaces*, Journal of Computational Physics, 227 (2008), pp. 1943–1961.
- [43] V. SHANKAR, G. B. WRIGHT, AND A. NARAYAN, *A robust hyperviscosity formulation for stable RBF-FD discretizations of advection-diffusion-reaction equations on manifolds*, SIAM Journal on Scientific Computing, 42 (2020), pp. A2371–A2401.
- [44] R. SHI, B. WANG, Z. YAN, Z. WANG, AND L. DONG, *Effect of surface topography parameters on friction and wear of random rough surface*, Materials, 12 (2019), p. 2762.
- [45] B. SJODIN, *How to generate random surfaces in COMSOL multiphysics®*. <https://www.comsol.com/blogs/how-to-generate-random-surfaces-in-comsol-multiphysics/>.
- [46] P. SUCHDE AND J. KUHNERT, *A meshfree generalized finite difference method for surface PDEs*, Computers & Mathematics with Applications, 78 (2019), pp. 2789–2805.
- [47] Z. SUN, W. GAO, AND R. YANG, *A convergent iterated quasi-interpolation for periodic domain and its applications to surface PDEs*, Journal of Scientific Computing, 93 (2022), p. 37.
- [48] Z. TANG, Z. FU, M. CHEN, AND L. LING, *A localized extrinsic collocation method for Turing pattern formations on surfaces*, Applied Mathematics Letters, 122 (2021), p. 107534.
- [49] TASNIM. <https://www.tasnimnews.com/fa/news/1394/09/15/935574/>.
- [50] A. M. TURING, *The chemical basis of morphogenesis*, Philosophical Transactions of the Royal Society B, 237 (1952), pp. 37–72.